# Impact of East Asian Summer Monsoon Heating on the Interannual Variation of the South Asian High

PENGFEI ZHANG*

*State Key Laboratory of Numerical Modeling for Atmospheric Sciences and Geophysical Fluid Dynamics, Institute of Atmospheric Physics, Chinese Academy of Sciences, and University of Chinese Academy of Sciences, Beijing, China*

YIMIN LIU AND BIAN HE

*State Key Laboratory of Numerical Modeling for Atmospheric Sciences and Geophysical Fluid Dynamics, Institute of Atmospheric Physics, Chinese Academy of Sciences, and Joint Center for Global Change Studies, Beijing, China*

(Manuscript received 9 February 2015, in final form 21 October 2015)

ABSTRACT

Occupying the upper troposphere over subtropical Eurasia during boreal summer, the South Asian high (SAH) is thought to be a regulator of the East Asian summer monsoon (EASM), which is particularly important for regional climate over Asia. However, there is feedback of the condensational heating associated with EASM precipitation to SAH variability. In this study, interannual variation of SAH intensity and the mechanisms are investigated. For strong SAH cases, the high pressure system intensifies and expands. Significant positive anomalies of the geopotential height and upper-tropospheric temperature were found over the Middle East and to the east of the Tibetan Plateau (TP), namely, the western and the eastern flanks of the SAH. The dynamical diagnosis and the numerical experiments consistently show that the interannual variation of SAH intensity is strongly affected by EASM precipitation over the eastern TP–Yangtze River valley. The feedback of the condensational heating anomaly to the SAH is summarized as follows: Excessive EASM heating excites a local anticyclone in the upper troposphere and warms the upper troposphere, leading to the eastward extension of the SAH's eastern edge and reinforcing geopotential height anomalies over East Asia. Furthermore, the monsoonal heating excites a westward-propagating Rossby wave that increases the upper-tropospheric geopotential height and warms the upper troposphere over the Middle East. In conclusion, this study suggests a mechanistic paradigm in which the EASM may also be a modulator of SAH variation rather than just a passive result of the latter as traditionally thought. The results suggest that the EASM and the SAH are a tightly interactive system.

## 1. Introduction

The South Asian high (SAH, or Tibetan high) is a large-scale anticyclonic system in the upper troposphere of subtropical Eurasia. Its center is located at the southern slope of the Tibetan Plateau (TP) in boreal summer (Fig. 1). In the North Hemisphere, the SAH is the strongest and most persistent upper-tropospheric circulation system besides the polar vortex (Mason and Anderson 1963). Its activities influence not only the weather and climate over Asia (Tao and Zhu 1964; Zhang and Wu 2001) but also the distribution and variability of trace constituents and aerosol in the upper troposphere and the lower stratosphere (Dethof et al. 1999; Fu et al. 2006; Park et al. 2008; Randel and Park 2006).

The formation and maintenance of SAH has been attributed to the summer diabatic heating over TP (Flohn 1957; Reiter and Gao 1982; Yanai et al. 1992; Yeh et al. 1957), condensational heating associated with the South Asian summer monsoon (Chen et al. 1987; Liu et al. 2001; Qian et al. 2002) and the East Asian summer monsoon

Denotes Open Access content.

* Current affiliation: Department of Earth, Atmospheric, and Planetary Sciences, Purdue University, West Lafayette, Indiana.

*Corresponding author address*: Dr. Yimin Liu, LASG, Institute for Atmospheric Physics, Chinese Academy of Science, P.O. Box 9804, Beijing 100029, China.
E-mail: lym@lasg.iap.ac.cn

DOI: 10.1175/JCLI-D-15-0118.1

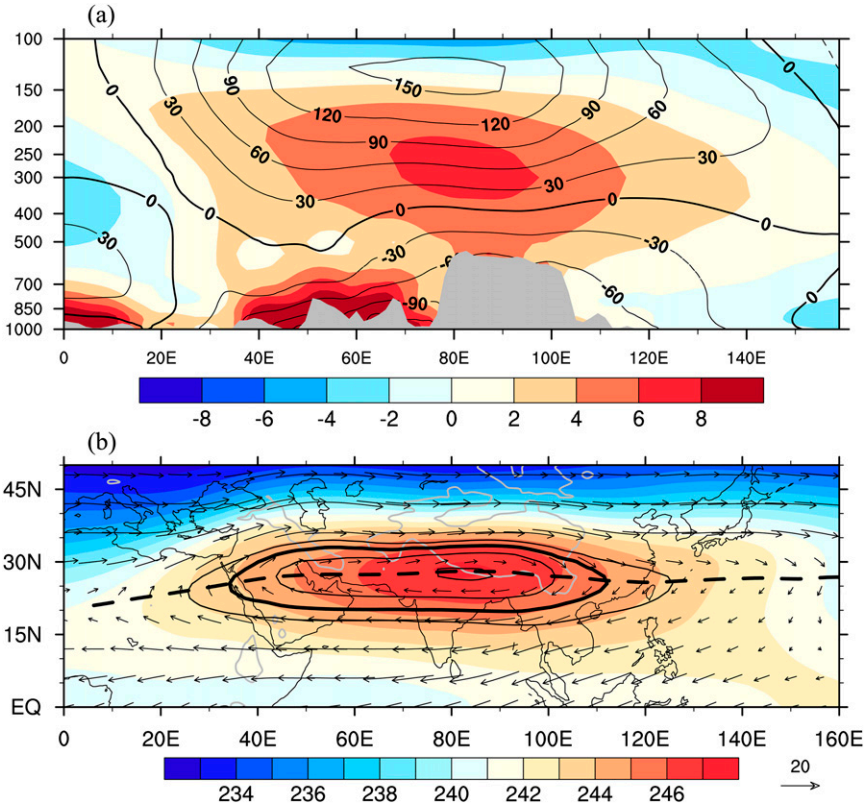


FIG. 1. Climatology of summertime SAH in 1979–2012: (a) vertical cross section averaged between 28° and 31°N of deviation from zonal mean for geopotential height (contours, gpm) and temperature (shaded, K); (b) geopotential height (contours, interval is 20 gpm) and wind (vectors, m $s^{-1}$) at 200 hPa and weighted average of upper-tropospheric temperature (400–200 hPa) (shaded, K). The thick black contour in (b) is the 12 520-gpm isoline. Dashed contour in (b) is the climatological ridgeline of SAH at 200 hPa. Gray shading in (a) denotes the topography. Gray contours in (b) delineate the topographic boundary of 1500 m.

(EASM) (Wu et al. 2015), and the existence of land–sea distribution along with large terrain (Wu and Liu 2003; Wu et al. 2009).

The variations of SAH and the related climatic impacts have long been an attractive topic. Existing studies mainly focus on two aspects: the location of the SAH center and the intensity of the SAH. For the former aspect, the location of the SAH center usually varies in the east–west direction, known as ''bimodality'': the Tibetan type (or eastern pattern) is when the center is located at the southern slope of the TP and the Iranian type (or western pattern) is when the center is located at the Plateau of Iran (IP). These two SAH types are associated with apparently different circulation at multiple time scales ranging from a few days to submonthly and interannual scales (Krishnamurti 1973; Liu et al. 2007; Luo et al. 1982; Wei et al. 2014; Zhang et al. 2014; Zhang et al. 2002), which has been linked to extreme weather and climate events in Asia (Ye and Gao 1979). For the latter aspect, the SAH intensity is also linked to summer extreme climate events and rainfall anomalies over Asia and over western Africa, the North Pacific, and Central America, especially at interannual scales (Kanamitsu and Krishnamurti 1978; Zhang et al. 2005; Zhao et al. 2007). In addition, studies suggested that the SAH intensity is influenced by climate modes over the tropical Pacific and Indian Oceans. For example, the summer SAH tends to be intensified following El Niño events (Zhao et al. 2009). In boreal summer, the positive tropical Indian Ocean (TIO) sea surface temperature anomalies (SSTA) following El Niño events warm the tropospheric temperature around the Indian Ocean and result in the intensification of the SAH (Huang et al. 2011; Qu and Huang 2012; Yang et al. 2007).

Previous studies suggested that the SAH variations could affect the EASM. In the subtropics, a strong and

eastward-expanding upstream SAH at the upper troposphere is ordinarily accompanied by the downstream western North Pacific subtropical high (WNPSH) stretching westward at low level and hence influencing EASM precipitation anomalies over eastern China (e.g., Jiang et al. 2011; Ren et al. 2007; Tao and Zhu 1964; Tao and Ding 1981). Such in-phase movements of the two circulation systems might be related to subtropical wave energy dispersion in the upper troposphere, which favors an intensified SAH over East Asia. Consequently, the descending motion and the adiabatic warming lead to the strengthening of the WNPSH in the lower troposphere and result in anomalies of the EASM (Ren et al. 2007; Tao and Wei 2006; Zhao et al. 2009).

The condensational heating released by EASM precipitation also feeds back to the maintenance of upper-tropospheric circulation (Jin et al. 2013; Liu et al. 2004; Lu and Lin 2009). Recently, Sugimoto and Ueno (2012) reported that the convective rainband over the eastern Tibetan Plateau to central-eastern China, where the main rainband of the EASM is located, is leading the SAH's reinforcement and eastward expansion in a time scale of a few days. Wu et al. (2015) suggested an inherent subtropical temperature–diabatic heating ($T$–$Q_z$) mechanism in which EASM precipitation contributes to the decadal variations of the SAH warm center. Another recent study found that the condensational heating related by precipitation over the Yangtze River valley can influence the horizontal shifts of the SAH (Wei et al. 2015). These studies indicate that precipitation over East Asia may also feedback to the SAH in addition to previous studies that emphasize the effects of the upper SAH on the EASM and precipitation. It is still unclear whether the EASM influences the variation of SAH intensity at interannual scales. If the EASM influences the SAH at interannual scales, then what is the possible mechanism? The present study will clarify this issue by investigating the feedback of EASM precipitation anomalies to the upper SAH at interannual time scales though statistical analysis, dynamic diagnosing, and numeric model experiments.

The rest of the paper is organized as follows. The data and methods are described in section 2. The year-to-year variation of SAH intensity and its relationship with the EASM are presented in section 3, and the associated mechanism in which the EASM impacts the SAH is explored in section 4. In section 5, numerical experiments are conducted to verify the rendered mechanism. Section 6 is devoted to conclusions and further discussion.

## 2. Data, method, and model

### *a. Datasets and methods*

The European Centre for Medium-Range Weather Forecasts interim reanalysis (ERA-Interim) is adopted to represent atmospheric circulation, whose horizontal resolution is 1.5° × 1.5° with 37 vertical levels (Dee et al. 2011). The sea surface temperature (SST) data are from the National Oceanic and Atmospheric Administration (NOAA) Extended Reconstructed SST (ERSST), version 3b, at 2° × 2° resolution (Smith et al. 2008). Precipitation data are obtained from the Global Precipitation Climatology Centre (GPCC) monthly dataset, version 6, at 0.5° × 0.5° horizontal resolution for the period 1979–2012 (Schneider et al. 2014). We also used rain gauge data from 572 stations in China for the period 1979–2008 from the National Meteorological Information Center, China Meteorological Administration.

This study focuses on boreal summer season—that is, June–August (JJA)—for the period 1979–2012. The seasonal mean is calculated using monthly and daily data. The least squares linear trend is removed from each variable to emphasize the interannual variation. All indices in this study are normalized.

The 200-hPa geopotential height is chosen to study the interannual variation of the SAH. The ridgeline of the SAH is where easterly flow reverses to westerly (Liu and Wu 2004). Thus, it mathematically fulfills $u = 0$ and $\partial u/\partial y > 0$. Here, $u$ is the zonal component of the wind. The 12 520-gpm isoline is employed as a reference line to represent the area of the SAH (Fig. 1b). The east ridge and west ridge are defined as the intersecting points between the 12 520-gpm isoline and the defined ridgeline. The intensity of the SAH is defined as the weighted sum of the geopotential height of all grid points, which is greater than 12 520 gpm and is physically equivalent to the index defined by Qian et al. (2002) and Qu and Huang (2012) at 100 hPa. The SAH index (SAHI) can represent the intensity and area of the SAH. The diagnoses to other geopotential height isolines and other isobaric surfaces show that the choice of reference isolines or isobaric surfaces is not sensitive.

In this paper, we use the EASM index (EASMI), defined as the difference between the area-averaged zonal wind anomalies at 850 hPa in a southern box (5°–15°N, 90°–130°E) and a northern box (22.5°–32.5°N, 110°–140°E) (as marked in Fig. 4d) following Wang and Fan (1999), and reverse it for facility. The TIO SSTA time series is defined as the weighted area average for 20°S–20°N, 40°–100°E following Qu and Huang (2012) and Xie et al. (2009).

Based on ERA-Interim daily datasets, the apparent heat source $Q_1$, the apparent moisture sink $Q_2$,

and their column integration $\langle Q_1 \rangle$ and $\langle Q_2 \rangle$ are calculated following Yanai et al. (1973) and Luo and Yanai (1984):

$$Q_1 = c_p \left[ \frac{\partial T}{\partial t} + \mathbf{v} \cdot \nabla T + \left( \frac{p}{p_0} \right)^{\kappa} \omega \frac{\partial \theta}{\partial p} \right], \quad (1)$$

$$Q_2 = -L \left[ \frac{\partial q}{\partial t} + \mathbf{v} \cdot \nabla q + \omega \frac{\partial q}{\partial p} \right], \quad (2)$$

$$\langle Q_1 \rangle = \frac{1}{g} \int_{p_t}^{p_s} Q_1 dp, \quad \text{and} \quad (3)$$

$$\langle Q_2 \rangle = \frac{1}{g} \int_{p_t}^{p_s} Q_2 dp, \quad (4)$$

where $T$ is temperature; $\theta$ is potential temperature; $q$ is specific humidity; $\mathbf{V}$ is the horizontal wind vector; $\omega$ is the vertical velocity in pressure coordinates; $\kappa = R/c_p$, where $R$ and $c_p$ are the gas constant and the specific heat at constant pressure of dry air, respectively; $L$ is the latent heat of condensation; $p_0 = 1000$ hPa; and $p_s$ and $p_t$ are the surface pressure and 100 hPa, respectively.

### b. Model

Two kinds of general circulation models are employed in this study. One is a dry linear baroclinic model (LBM) based on primitive equations (Watanabe and Kimoto 2000). The horizontal resolution of the model uses spectral triangular truncation at wavenumber 42 (T42). This model has 20 vertical levels on a sigma coordinate system. In addition to vertical diffusion, biharmonic horizontal diffusion having a time scale of 6 h is also employed. Rayleigh friction and Newtonian damping are applied with a time scale of $(0.5 \text{ day})^{-1}$ for $\sigma \geq 0.9$, $(1 \text{ day})^{-1}$ for $\sigma \leq 0.3$, and $(20 \text{ day})^{-1}$ elsewhere (Lu and Lin 2009). The 1961–90 summertime climatology obtained from ERA-40 is employed as the basic state. A condensational heating anomaly is prescribed in the linearized temperature equation to examine the responses of atmospheric circulation. The model is integrated for 30 days and the quasi-steady state is approached after day 15. The circulation fields are averaged between day 25 and day 29 to designate the steady response to the prescribed diabatic heating. A detailed description of the abovementioned mathematical principles of linear dynamics can be found in Watanabe and Kimoto (2000).

The AGCM used in this study is the Spectral Atmospheric Model of the IAP/LASG, version 2.4 (SAMIL2), developed at LASG/IAP (Bao et al. 2010), which can reasonably simulate the East Asian monsoon and subtropical high (Bao et al. 2013; Liu et al. 2013; Wu et al. 2012). This model applies the Tiedtke convection scheme (Tiedtke 1989), in which the thermodynamic forcing by convection is governed by the following equation:

$$\frac{\partial \overline{s}}{\partial t} + \mathbf{v} \cdot \nabla \overline{s} + \overline{w} \frac{\partial \overline{s}}{\partial z} = -\frac{1}{\overline{\rho}} \frac{\partial}{\partial z} (\overline{\rho}\, \overline{w's'}) + L(\overline{c} - \overline{e}) + \overline{Q_R}, \quad (5)$$

where $s = C_p T + gz$ is the dry static energy, $\rho$ is the density of air, $\mathbf{v}$ is the horizontal wind velocity, $w$ is the vertical velocity, $c$ is the rate of condensation, $e$ is the rate of evaporation, and $Q_R$ is the radiative heating. The overbar denotes an area average that is large enough to contain an ensemble of cumulus clouds, and the prime denotes deviations from the area average. To conduct the sensitivity experiment, we added a term $F$, which presents the enhanced condensational heating on the right-hand side of the equation with spatial and vertical distribution. The extra term $F$, which is the same as condensational heating prescribed in LBM, is added in the key region during June–August. Both the control and sensitivity experiments are integrated for 10 years, and the results from the last five years are extracted for the comparison studies showing the difference between the sensitivity experiment and the control run.

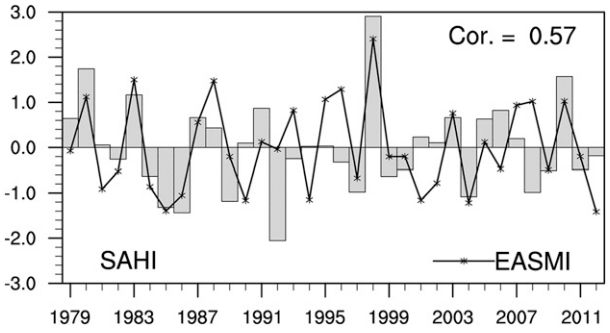


FIG. 2. Normalized SAHI (gray bars) and the EASMI (black line with asterisks).

## 3. Interannual variation of SAH intensity and its relationship with EASM

### a. Characteristics of interannual variation of SAH intensity

The interannual variation of SAHI is shown in Fig. 2. Years with normalized SAHI above 0.8 (below −0.8) standard deviation are employed to present the stronger (weaker) SAH years. During 1979–2012, five years (1980, 1983, 1998, 2006, and 2010) and seven years (1985, 1986, 1989, 1992, 1997, 2004, and 2008) are identified as strong and weak SAH years, respectively. Consistent with our definition of SAHI in section 2, in the years with stronger-than-normal (weaker than normal) SAH,

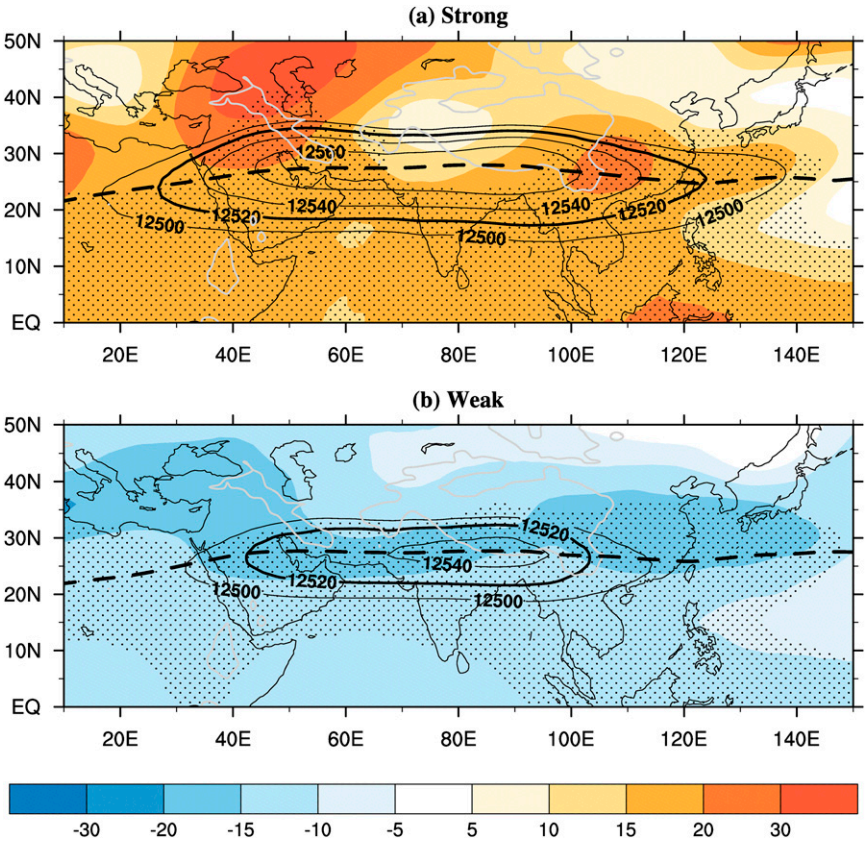


FIG. 3. Composite 200-hPa geopotential height (gpm) in (a) strong SAHI years and (b) weak SAHI years. The contours are mean geopotential height for two cases. The shading indicates geopotential height anomalies relative to climatology for those two cases, respectively. Stippled areas denote the 95% confidence level for geopotential height anomalies. Dashed lines are ridgelines of SAH for those two cases, respectively. Gray contours delineate the topographic boundary of 1500 m.

the area occupied by SAH is larger (smaller), and the 200-hPa geopotential height over the SAH center is higher (lower) than that in normal years (Figs. 3a,b). In those two cases, both centers of the SAH are located at the southern slope of Tibetan Plateau with a difference in geopotential height of approximately 30 gpm.

In strong SAH years, the east ridge of the SAH extends more than 20° eastward to the East China Sea and the west ridge of the SAH extends westward by about 15° to North Africa compared to that in the weak SAH years. It is noteworthy that the geopotential height anomalies are not apparent in the northern flank of the SAH center in strong SAH years. In addition, significant increases in the geopotential height are also noticed south of the SAH, including the tropics. In weak SAH years, however, the negative geopotential height anomalies prevail over subtropical Eurasia, especially along the SAH ridgeline.

Overall, between the strong and weak SAHI cases, the most significant geopotential anomalies are aligned in the eastern TP to eastern China and the Middle East to the IP. As a result, the eastern and western boundaries of the SAH expand significantly, while the northern and southern boundaries do not.

### *b. Relationship between EASM and SAH intensity*

Previous studies have shown that the variation of summer precipitation over eastern China is sensitive to SAH variability and is mainly through the variation of the WNPSH at multiple scales, ranging from synoptic to decadal scales (e.g., Jiang et al. 2011; Sugimoto and Ueno 2012; Tao and Zhu 1964; Tao and Wei 2006; Wu et al. 2015; Zhang et al. 2005; Zhang and Wu 2001; Zhao et al. 2009). Circulation anomalies associated with the east–west shift of the SAH can also directly induce the vertical motion anomalies over eastern China and contribute to the rainfall anomalies (Wei et al. 2014). We especially investigate the linkages between SAH intensity and East Asia summer precipitation at interannual scales in this study (Fig. 4).

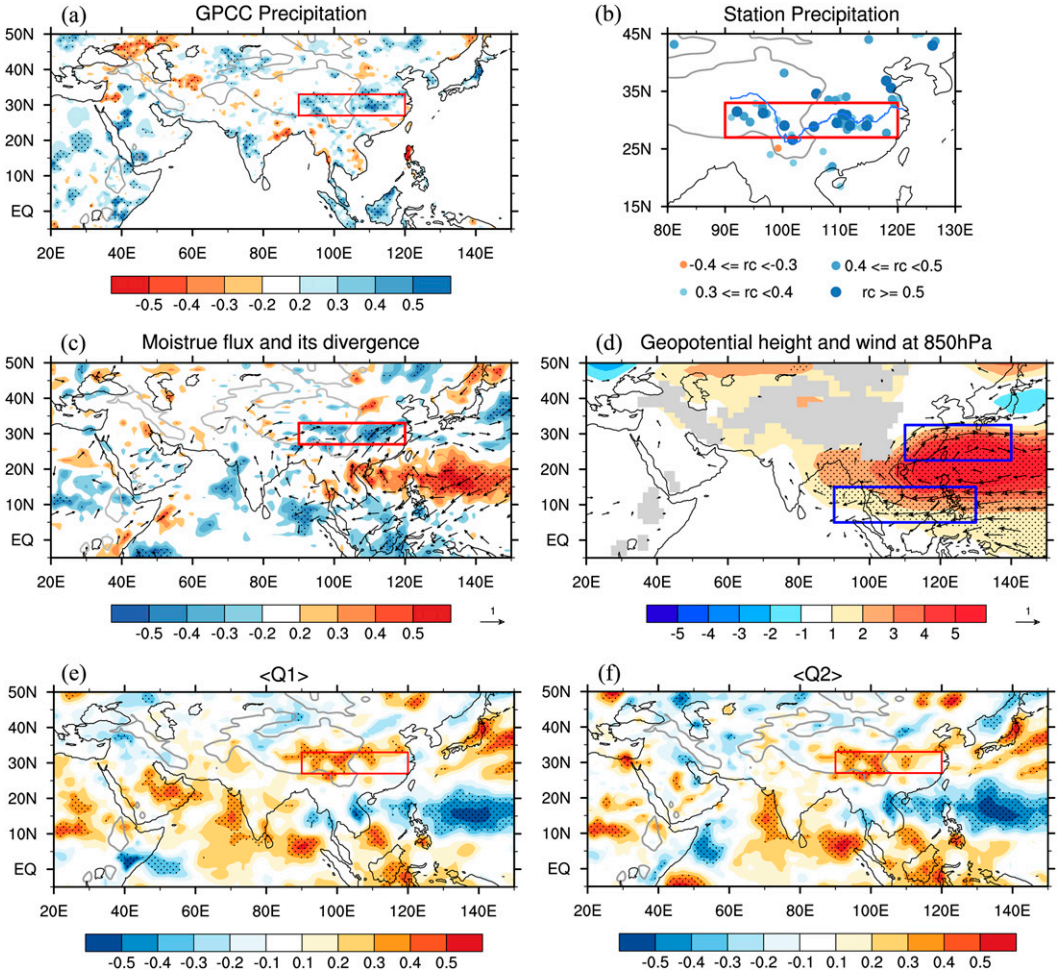


FIG. 4. Regressions of (a) precipitation, (b) station precipitation in China, (c) integrated moisture flux and its divergence, (d) 850-hPa geopotential height (gpm) and wind ($m\,s^{-1}$), (e) $\langle Q_1 \rangle$, and (f) $\langle Q_2 \rangle$ onto SAHI. Precipitation, moisture flux, and $\langle Q_1 \rangle$ and $\langle Q_2 \rangle$ are normalized before calculating the regression coefficients to facilitate the comparison of precipitation variability in the study area. Red boxes highlight the key region of precipitation anomalies (27°–33°N, 90°–120°E). Blue boxes in (d) show the domain used to define the EASMI. Stippled areas are the grid cells where regression coefficients are significant at the 95% confidence level. In (b), stations with regressed precipitation significant at the 95% confidence level are shown. In (c) and (d), only regression coefficients of vectors at the 95% confidence level are shown. Gray shading in (d) and gray contours in (a)–(c),(e), and (f) delineate the topographic boundary of 1500 m. The calculation of regression coefficients is from the period 1979–2012, except the rain gauge data in (b) is 1979–2008.

Figure 4a presents the regressed precipitation upon the SAHI. With a strong SAH, excessive rainfall tends to occur over the eastern Tibetan Plateau and the Yangtze River valley (27°–33°N, 90°–120°E; hereinafter the T-Y region), while deficits in rainfall are around the Plateau of Iran (Fig. 4a). This spatial pattern of rainfall change over eastern China is also verified by the China Meteorological Administration station observations as shown in Fig. 4b.

Consistent with precipitation anomalies, excessive moisture is transported to and converges in the T-Y region as a result of the enhanced southwesterly flow in strong SAH years (Fig. 4c). The enhanced southwesterly flow is closely linked to an anomalous anticyclone along the western edge of the WNPSH (Figs. 4c,d). The patterns of precipitation and low-level circulation in East Asia are the behavior of the leading EOF mode of the EASM (Huang et al. 2012; Wang et al. 2008). Specifically, as the east edge of the SAH expands eastward during strong SAH years, the WNPSH extends westward at the lower layer, known as ''moving in the opposite direction'' phenomenon (Tao and Zhu 1964). In contrast, along the western flank of the SAH, anomalous moisture divergence occurs over western Asia, caused

TABLE 1. Correlation coefficients between SAHI and EASMI, TYP, TIO, and Niño-3.4. One (two) asterisk(s) denotes the 95% (99%) confidence level.

| | Correlation | | | | Partial correlation (excluded third index) | | |
|---|---|---|---|---|---|---|---|
| | TYP | EASMI | TIO | Niño-3.4 | TYP (EASMI) | EASMI (TIO) | EASMI (Niño-3.4) |
| SAHI | 0.54** | 0.57** | 0.58** | 0.56** | 0.26 | 0.38* | 0.37* |

by divergence motion, leading to negative precipitation anomalies there (Figs. 4a,c).

Above-normal precipitation over the eastern Tibetan Plateau and the Yangtze River valley has been attributed to an active EASM (Chang et al. 2000a,b; Wang et al. 2008). The correlation between the EASMI and the T-Y region precipitation is 0.67, significant at the 99% confidence level, during 1979–2012. This study further shows that the excessive rainfall and the active EASM concur with a strong SAH at interannual scales.

The relationship between the SAH, the eastern Tibetan Plateau, and the Yangtze River Valley precipitation (TYP) and the EASM is quantified using correlation analysis (Table 1). Specifically, the correlation coefficient between the SAHI and TYP is 0.52 and between the SAHI and the EASMI is 0.57, significant at the 99% confidence level. The partial correlation coefficient between the SAHI and TYP, while not considering the contribution of the EASMI, decreases to 0.26 (not significant), since the EASM and precipitation over the T-Y region are within one dynamical system.

Previous studies also indicated that the preceding El Niño events and the following summer warm SSTA in the TIO following El Niño events can intensify the SAH and then the EASM (Huang et al. 2010, 2011; Wu et al. 2010; Xie et al. 2009; Zhang et al. 1999; Zhao et al. 2009). To test whether the significant relationship between the SAH and the EASM identified above is driven by El Niño and TIO warm events, partial correlation between the SAHI and the EASMI excluding the contributions of El Niño (presented as the Niño-3.4 index) and the TIO SSTA was investigated (Table 1). The partial correlation coefficients (0.37 and 0.38, respectively), although lower than the original value (0.57), are still significant at the 95% confidence level. This suggests that the relationship between the SAH and the EASM is generally robust, while the preceding El Niño events and the simultaneous warm events of TIO could strengthen their linkage.

In addition to the contribution of the SAH to EASM precipitation variability found by many previous studies (e.g., Ren et al. 2007; Tao and Zhu 1964; Tao and Ding 1981), as a warm high dominating the upper troposphere, the SAH and its variation are strongly influenced by atmospheric condensational heating released by precipitation over East Asia (Liu et al. 2012; Wu et al. 2015). To explore the possible dynamics of the interannual variation of SAH intensity, diabatic heating due to EASM precipitation was analyzed. Here, the total diabatic heating is calculated as the column-integrated apparent heat source $\langle Q_1 \rangle$, which is the sum of sensible heating, net radiation, and condensational heating. In addition, the condensational heating associated with precipitation is represented by $\langle Q_2 \rangle$, the integrated apparent moisture sink, following Luo and Yanai (1984).

Figures 4e and 4f show the relationship between the SAH and $\langle Q_1 \rangle$ and $\langle Q_2 \rangle$, respectively. Generally, a strong SAH is accompanied by positive anomalies in $\langle Q_1 \rangle$ over the T-Y region and negative anomalies over the western North Pacific (WNP), indicating an increased (decreased) heat release into the atmosphere over the T-Y (WNP) region (Fig. 4e). Furthermore, these $\langle Q_1 \rangle$ anomalies are mainly contributed to $\langle Q_2 \rangle$, which is associated with EASM precipitation anomalies over the T-Y and WNP regions (Figs. 4a,f). In these regions, precipitation anomalies and the diabatic heating release are tightly linked to the EASM circulation in the lower troposphere. Negative $\langle Q_2 \rangle$ anomalies over the eastern IP consist of local precipitation decreases. The distribution of negative anomalies of $\langle Q_1 \rangle$ is different from that of $\langle Q_2 \rangle$ over the Middle East (i.e., the western flank of SAH), indicating the longwave radiation and sensible heat anomalies (Figs. 4e,f).

The changes in diabatic heating can feed back to the upper-tropospheric circulation (Liu et al. 2004, 2001; Lu and Lin 2009). Thus, we hypothesize that, in addition to the contribution of the SAH variation to EASM precipitation proposed in previous studies, the interannual variation of SAH is subjected to changes in the EASM precipitation and the associated diabatic heating. This hypothesis is tested by diagnosing the related dynamic and thermodynamic processes and performing numerical experiment in the following sections. In addition, during strong SAHI years, there is significant condensational heating released over the north tropical Indian Ocean (i.e., to the south of the SAH). Contributions of diabatic heating in these regions to the interannual variation of the SAH will also be investigated in numerical experiments.

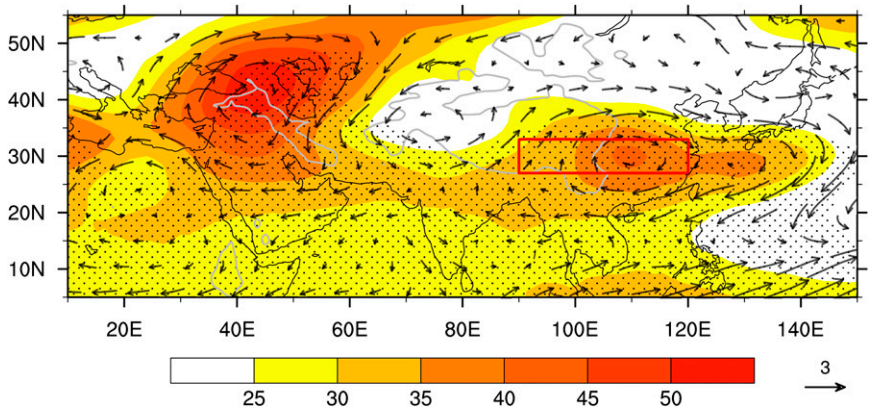


FIG. 5. Composite differences between the strong and weak SAHI years for wind (vectors, m s$^{-1}$) and geopotential height at 200 hPa (shaded, gpm). Stippled areas are the grid cells where composite geopotential height anomalies are significant at the 95% confidence level. The red box shows the T-Y region. Gray contours delineate the topographic boundary of 1500 m.

## 4. SAH intensity variation influenced by EASM

According to the abovementioned analysis, an anomalously strong SAH corresponds to excessive condensational heating released over the T-Y region, which is attributable to lower-tropospheric moisture convergence associated with the EASM circulation. The mechanism responsible for the linkage between EASM precipitation and SAH intensity will be explore in this section.

The relationship between circulation and diabatic heating can be explained by potential vorticity (PV) balance. In the vicinity of the SAH ridgeline, the zonal advection of vorticity is relatively weak. The responses of free atmosphere to diabatic heating can be depicted by the vertical distribution of diabatic heating according to the vorticity balance. Specifically, condensational heating released from precipitation tends to induce negative (positive) vorticity and anticyclonic (cyclonic) circulation in the upper (lower) troposphere (Liu et al. 2004; L. Wang et al. 2013; Wu and Liu 2000; Wu et al. 2009). Figure 5 shows the differences in the geopotential height and wind anomalies at 200 hPa between the strong and weak SAH cases. Consistent with vorticity balance, condensational heating released from precipitation anomalies over the T-Y region are accompanied by an anomalous anticyclone in the upper troposphere. The northerly wind anomalies along the eastern portion of the anticyclone are located over eastern China, indicating the eastward expansion of the east edge of the SAH. Enhanced geopotential height anomalies over East Asia also represent the reinforcement of the eastern part of the SAH.

The wind anomalies are parallel to isobars, which indicate that the upper anomalous circulation is geostrophic (Fig. 5). Along with this anomalous anticyclone over the eastern flank of the SAH, due to the $\beta$ effect, a geostrophic Rossby wave train is observed spanning from East Asia to the Middle East over the subtropics and midlatitudes: an anomalous trough centered on 70°E together with an anomalous anticyclone in the Middle East. The former prevents the increase of the geopotential height over north of the SAH center. The latter favors the westward expansion of the SAH over the Middle East in strong SAH years (Fig. 3a). This Rossby wave train may be excited by the diabatic anomalies related to monsoon and causes a remote response east of the Mediterranean Sea and the Middle East (Rodwell and Hoskins 1996). The Rossby wave response will be further discussed in the following sections and verified by numerical experiments in section 5.

The differences in the vertical structure of the temperature, the meridional wind, and the vertical motion along the subtropics between strong and weak SAHI years are presented in Fig. 6. Warm anomalies are aligned in the T-Y region accompanied with ascending movement in the eastern heating and descending movement in the western heating. Also a local anticyclonic anomaly is located in the upper troposphere. West of the SAH, an anomalous northerly wind over the IP and an anomalous southerly wind over the east coast of the Mediterranean Sea form another anomalous anticyclone. This anticyclone and warm temperature anomalies in the western part of the SAH are related to the westward-propagating Rossby wave linked to the condensational heating anomalies over the T-Y region. The results is consistent with Rodwell and Hoskins (1996), who demonstrated that the interaction between a South Asian monsoon–induced westward-propagating Rossby wave and the midlatitude westerly wind can account for the warming and adiabatic descent over the

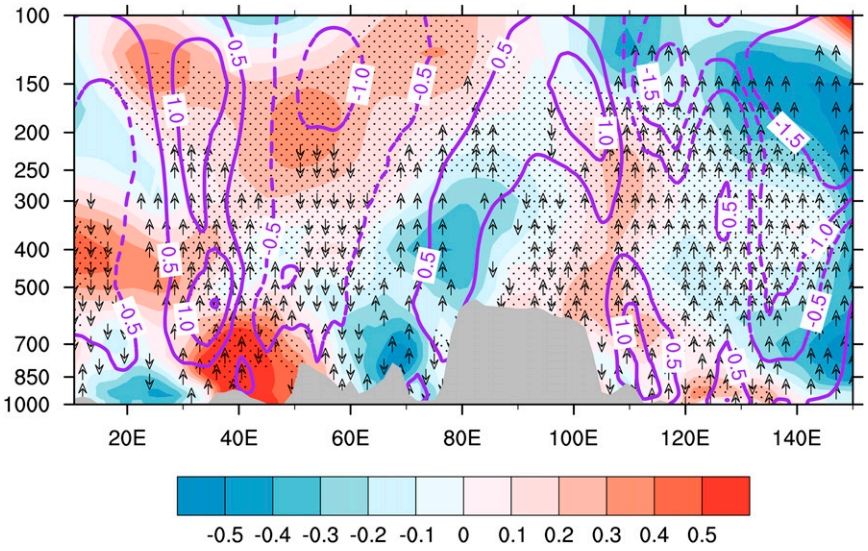


FIG. 6. Cross section averaged between 28° and 31°N of composite differences between strong and weak SAHI years for temperature deviation from the corresponding zonal means of 20°–150°E (shaded, interval is 0.1 K), meridional wind (purple contours, interval is 0.5 m s$^{-1}$ with zero lines omitted and negative values dashed), and vertical motion (vectors). Vectors indicate the direction of vertical motion where the absolute value exceeds 0.004 Pa s$^{-1}$. Stippled areas are the grid cells where temperature anomalies are significant at the 95% confidence level. Gray shaded areas highlight the topography.

Mediterranean Sea. The northerly wind anomalies over the IP accompanying subsiding airflow induced by westward-propagating Rossby wave can produce the adiabatic warming (Fig. 6), suppress the local precipitation (Figs. 4a,c,f), and increase the near-surface temperature (Fig. 6). The suppressed precipitation over the eastern IP decreases local condensational heating (Figs. 4a,f), which reinforces the adiabatic descent. Over the east coast of the Mediterranean Sea, the upper-tropospheric warm anomalies are mainly contributed by the southerly warm advection. However, anomalous dry convection accompanying the southerlies does not generate precipitation there. The adiabatic warming over the IP and warm advection over the east coast of the Mediterranean Sea occur in association with a barotropic blocking flow and are responsible for the upper-tropospheric warm anomalies over the western flank of the SAH during strong SAHI years. Those warming processes have been verified by the diagnosis of a thermodynamic energy equation (not shown). The combined dynamics and thermodynamic processes lead to warm anomalies over the Middle East and increase the geopotential height along the western edge of the SAH (Fig. 3a).

Based on the discussion above, the interannual variation of SAH intensity could be closely related to the condensational heating feedback of the precipitation anomalies over the eastern Tibetan Plateau and the Yangtze River valley associated with an active EASM. The feedback of diabatic heating associated with anomalous precipitation is linked to a local anticyclonic circulation favoring a strengthening of the SAH and an eastward expansion of the eastern part of the SAH. In addition, the EASM-induced diabatic heating anomalies also warm the upper troposphere, and thus increase the upper geopotential height. With the changes in upper-tropospheric circulation, a stationary Rossby wave is observed, propagates westward, warms the upper troposphere over the Middle East through adiabatic subsidence and warm advection, and favors the westward expansion of the SAH.

## 5. Numerical simulations: Influence of EASM precipitation on the interannual variation of the SAH intensity

To test the hypothesis in the previous section that the interannual variation of SAH intensity is associated with the EASM, a series of numerical simulations are performed and the results are discussed.

### *a. LBM experiment*

To understand the feedback of condensational heating to atmospheric circulation, an LBM is employed to examine the responses of circulation to EASM precipitation anomalies. The composite differences of $Q_2$

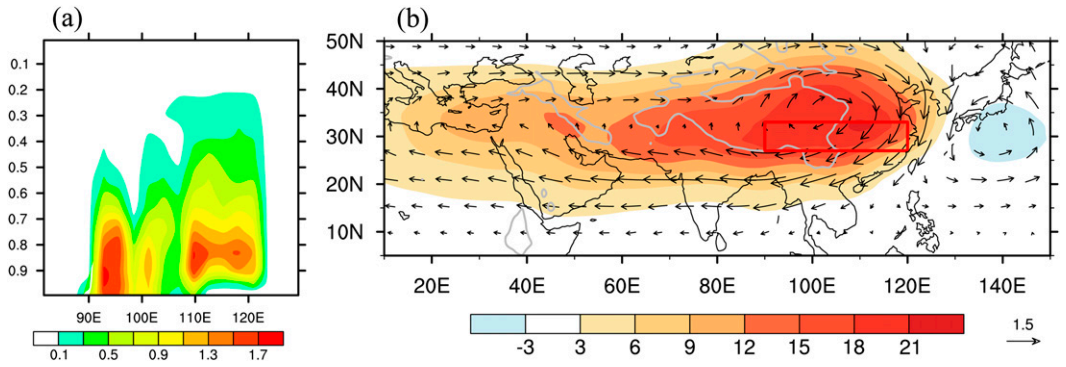


FIG. 7. (a) Vertical profile of condensational heating anomalies (K day$^{-1}$) along 30°E over the T-Y region. (b) For days 25–29, the mean responses of geopotential height (shaded, gpm) and wind (vectors, m s$^{-1}$) at 200 hPa to the condensational heating anomalies in the LBM run. The red box denotes the T-Y region in which the condensational heating is prescribed. Gray contours delineate the topographic boundary of 1500 m.

between strong and weak SAHI years are prescribed over the T-Y region (Fig. 7a).

Figure 7b shows the responses of 200-hPa circulation to the prescribed condensational heating anomalies in the LBM experiment. The results show that an anomalous anticyclone is generated over East Asia, due to the PV balance. The increases in 200-hPa geopotential height are most significant at the center of the T-Y region through geostrophic adjustment. The maximum response is centered on the eastern slope of the TP, where the eastern flank of the SAH is located. It indicates that the precipitation anomalies induced by an active EASM lead to the eastward expansion of the SAH. These responses of the geopotential height and the wind field occur not only around the forcing region but also in the broad subtropical regions to the west of the forcing. Although the geopotential height over the SAH area is enhanced in the LBM experiment, the signal over the western part of the SAH is weak compared to that in observations (Fig. 5). The geopotential height anomalies over there are even stronger than those over the eastern part of the SAH in observations. A possible reason is that the subsidence response accompanied with the Rossby wave over the eastern IP (40°–60°E) in the LBM experiment is too weak compared to that in observations and leads to a weaker adiabatic warming over there (not shown). We will further discuss the effects of subsidence over the eastern IP trough in the AGCM experiment.

The Rossby wave response diagnosed in observations can be confirmed by the time evolutions of the upper-tropospheric circulation in the LBM experiment (Fig. 8). The responses of the 200-hPa geopotential height are around the forcing region initially and then zonally propagate to the west in the following days with a propagating velocity of about 10 m s$^{-1}$. This wave propagates to the Middle East by day 6 and approaches the quasi-steady state around day 16. From day 21 forward, an independent geopotential height response center develops over the IP, but its intensity is relatively weak compared to that in observations (Figs. 3a and 5).

During strong SAHI years, there is significant condensational heating released at the northern tropical Indian Ocean (i.e., to the south of the SAH) (Fig. 4f). Its effects on the SAH are also investigated using the LBM. The results show that condensational heating at the northern tropical Indian Ocean favors the SAH extending equatorward rather than intensifying it (not shown). That is why the geopotential height south of the SAH, even over the TIO, is reinforced in strong SAHI years (Fig. 3a). The results are consistent with recent studies (Qu et al. 2015; Wei et al. 2012) that the southward shift of the SAH in a warming climate is mainly caused by increasing precipitation over the north Indian Ocean in observations and outputs from the phase 5 of the Coupled Model Intercomparison Project (CMIP5). Although the heating over the northern tropical Indian Ocean cannot intensify the SAH directly, it can contribute to the intensity of SAH indirectly through the changes in the lower-tropospheric flow. The heating over the northern tropical Indian Ocean is related to Indian summer monsoon activities that can influence the water vapor transport to eastern China from the Indian monsoon region, which has a close relation to the summer rainfall over the middle and lower reaches of the Yangtze River valley (Liu and Ding 2008; Zhang 2001). In fact, water vapor has been transported to the T-Y region from the northern tropical Indian Ocean (Figs. 4c,d).

### b. *AGCM experiment*

The responses of the upper geopotential height and circulation over the Middle East in the LBM run are

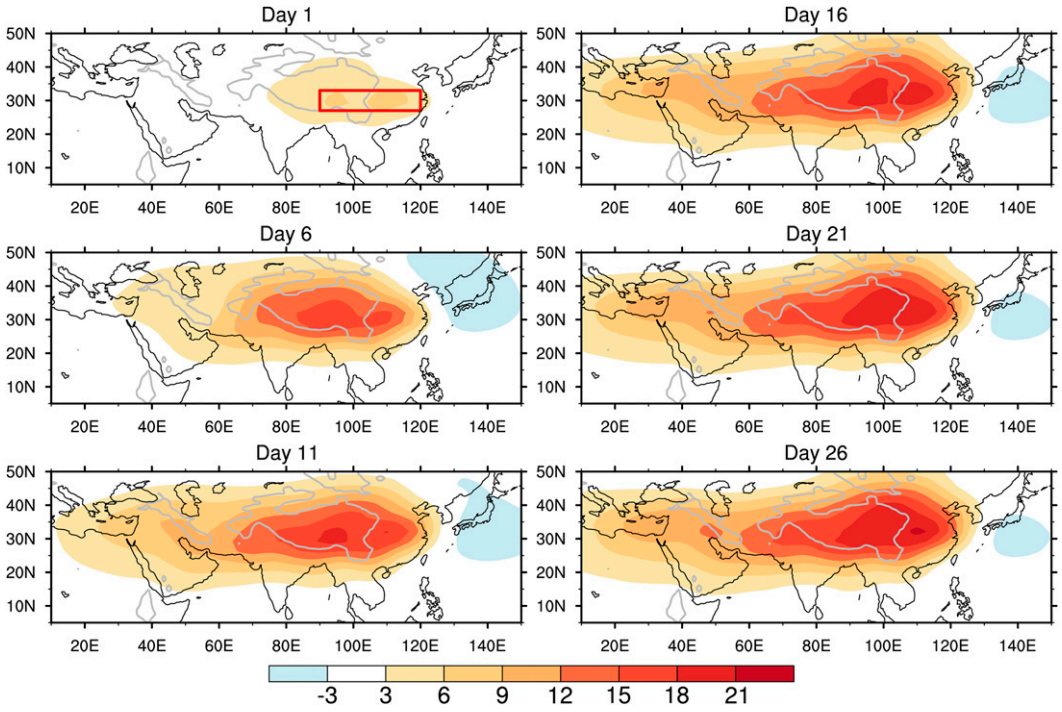


FIG. 8. Evolution of 200-hPa geopotential height response (gpm) to EASM condensational heating. The red box shows the T-Y region. Gray contours delineate the topographic boundary of 1500 m.

weaker than that in observations. The causes might be the weak vertical velocity response over the IP in the LBM experiment and the further diabatic processes, that is, the descending motion associated with the westward-propagating Rossby wave. The decent increases surface sensible heating and longwave radiation over the Middle East. Such further diabatic processes are not included in the linear model. Wu et al. (2015) indicate that the longwave radiation and sensible heating over western Asia also contribute to the formation and variation of the SAH. The longwave radiation is the response to the monsoonal convective heating to its east (Rodwell and Hoskins 1996; Rodwell and Hoskins 2001). To represent the impact of adiabatic subsidence and further diabatic processes, an AGCM that includes physical processes is implemented. The results show that the geopotential height at the eastern flank and western flank of the SAH is increasing in boreal summer when the condensational anomalies are prescribed in the T-Y region (Fig. 9a). The western part of the SAH is substantially enhanced and expands to the west when the subsidence response over the eastern IP (40°–60°E) is improved (Figs. 9a,b). It suggests that the adiabatic and diabatic processes caused by the westward-propagating Rossby wave over the Middle East strengthen the SAH to the west. As a result, the entire SAH system intensifies and expands when low-level EASM circulation is anomalously strong. The low-level circulation responses in East Asia in the AGCM experiment (Fig. 9c) share a similarity with that in observations (Fig. 4d), although the subtropical anticyclone over the western Pacific Ocean is weaker because of the fixed SST in the AGCM experiment. The distribution of the precipitation response in the AGCM experiment (Fig. 9c) is consistent with that in observations (Fig. 4a), especially outside the forcing region, which further verifies the results of the abovementioned analyses.

## 6. Conclusions and discussion

This study investigates the mechanisms responsible for the interannual variation of SAH intensity. In addition to the contribution of the SAH variation to East Asia precipitation, we provide evidence that the interannual variation of SAH intensity is also influenced by EASM latent heating. The key results are summarized as follows.

1) In a strong SAH year, the geopotential height in the SAH center is more than 30 gpm higher. The SAH covers a larger area from east of North Africa to the East China Sea. The significant positive anomalies of geopotential height are mainly located in two areas: the Middle East and from the eastern TP to eastern

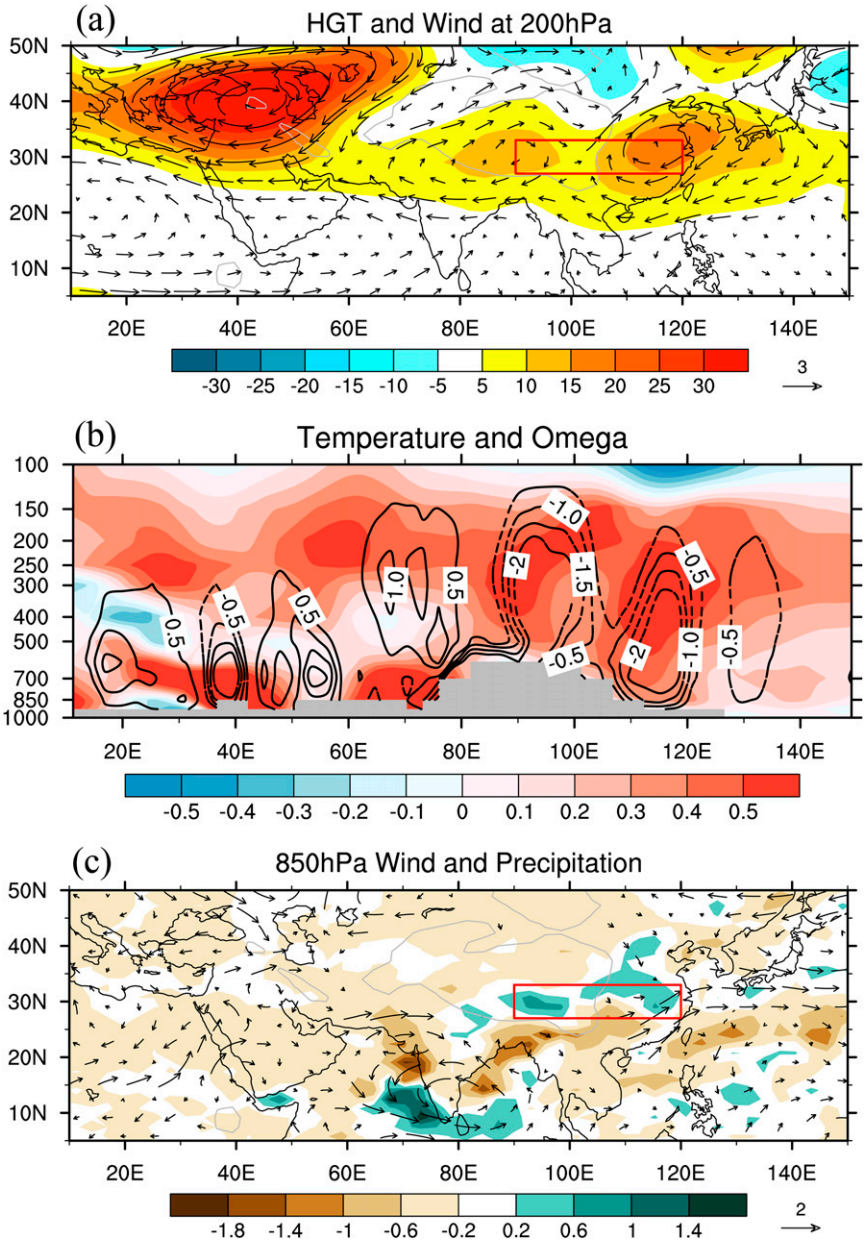


FIG. 9. Responses to EASM condensational heating in the AGCM experiment: (a) 200-hPa geopotential height (shaded, gpm) and wind (vectors, m $s^{-1}$), (b) height–longitude cross section averaged between 28° and 32°N of vertical velocity (contours, 0.01 Pa $s^{-1}$) and temperature (shaded, K) along 30°N, and (c) 850-hPa wind (vectors, m $s^{-1}$) and precipitation (shaded, mm $day^{-1}$). The responses are the differences between the sensitivity experiment and the control run. Red boxes show the T-Y region in which the condensational heating is prescribed. Gray contours in (a) and (c) delineate the topographic boundary of 1500 m. Gray shading in (b) denotes the topography.

China. The upper-tropospheric temperature increases in these areas as well, which favors the increases in geopotential height.

2) At interannual scales, SAH intensity is closely linked to condensational heating associated with precipitation anomalies over east TP–Yangtze River valley and the corresponding lower-tropospheric EASM circulation. In an active EASM year, more moisture is transported to central-eastern China along the western flank of the WNPSH and converges in the T-Y

region, increasing summer precipitation. The EASM, in turn, is highly correlated with SAH intensity. In contrast, precipitation was suppressed in western Asia, where the western flank of the SAH is aloft.

3) The condensational heating released by EASM precipitation plays an important role in the variation of the SAH. In the upper troposphere, the vertical distribution of condensational heating induces an anomalous anticyclone over subtropical East Asia in strong SAHI years from the review of vorticity balance. As a result, the east edge of the SAH extends farther eastward. The temperature anomalies related to T-Y region precipitation anomalies reinforce the upper-tropospheric geopotential height over the eastern TP and eastern China. The anomalously warm upper troposphere over the Middle East and the IP and the consequent geopotential height increasing are generated as a result of warm advection and adiabatic subsidence. The changes in Middle East and IP circulation are strongly linked to the westward-propagating Rossby waves excited by the condensational heating over East Asia, which further suppress the precipitation around the IP. Overall, the precipitation anomalies associated with the EASM can feed back to the SAH both thermodynamically and dynamically. The mechanism was verified by the sensitivity experiments from both the LBM and AGCM experiments. The upper-tropospheric anticyclonic circulation and the Rossby wave propagation are generated in numerical simulations by prescribing heating anomalies over the T-Y region. The results support our hypothesis that the interannual variation of SAH intensity is also influenced by the condensational heating associated with the EASM.

Previous studies suggested that the variation of the SAH could affect the WNPSH and the EASM precipitation (e.g., Ren et al. 2007; Tao and Wei 2006; Zhao et al. 2009). The results presented in this study demonstrate a mechanistic paradigm in which the EASM might be a modulator of SAH intensity rather than a passive response to the latter as traditionally thought. Combining our results with these existing studies, we suggest that the EASM and the SAH are tightly interactive systems in which one may influence the other.

Overall, this study focuses on the responses of upper-tropospheric circulation to EASM precipitation. There are several persistent oceanic phenomena that can influence the interannual variation of the SAH and the EASM, including preceding El Niño events, warm pool cooling, and TIO warming following El Niño events (Huang et al. 2010; Huang and Sun 1992; B. Wang et al. 2013, 2008; Wu et al. 2010; Wu and Liu 1995; Wu et al. 1995; Xie et al. 2009; Zhao et al. 2009). Our results show that the relationship between SAH intensity and the EASM is still significant without the contribution of tropical SSTA (such as the TIO). Whether the mechanism in which EASM influences SAH changes under different tropical ocean conditions (such as different El Niño types) merits further investigation. The impacts of decadal signals (including Pacific decadal oscillation) and other circulation modes (including Arctic Oscillation) on SAH variability will also be the focus of our future research.

*Acknowledgments.* The authors highly thank Dr. Jianhua Lu and Dr. Xiaocong Wang for the discussions that improved the manuscript. We appreciate Prof. Hoskins, Prof. Minfang Ting, Prof. Guoxiong Wu, Dr. Anmin Duan, and three anonymous reviewers for their insightful comments, and Dr. Laifang Li for her editorial assistance. This paper is supported by the National Natural Science Foundation of China (Grants 91437219 and 41275088) and the Third Tibetan Plateau Scientific Experiment (Grant GYHY201406001).

## REFERENCES

Bao, Q., G. Wu, Y. Liu, J. Yang, Z. Wang, and T. Zhou, 2010: An introduction to the coupled model FGOALS1.1-s and its performance in East Asia. *Adv. Atmos. Sci.*, **27**, 1131–1142, doi:10.1007/s00376-010-9177-1.

——, and Coauthors, 2013: The Flexible Global Ocean-Atmosphere-Land system model, Spectral Version 2: FGOALS-s2. *Adv. Atmos. Sci.*, **30**, 561–576, doi:10.1007/s00376-012-2113-9.

Chang, C.-P., Y. Zhang, and T. Li, 2000a: Interannual and interdecadal variations of the East Asian summer monsoon and tropical Pacific SSTs. Part I: Roles of the subtropical ridge. *J. Climate*, **13**, 4310–4325, doi:10.1175/1520-0442(2000)013<4310:IAIVOT>2.0.CO;2.

——, ——, and ——, 2000b: Interannual and interdecadal variations of the East Asian summer monsoon and tropical Pacific SSTs. Part II: Meridional structure of the monsoon. *J. Climate*, **13**, 4326–4340, doi:10.1175/1520-0442(2000)013<4326:IAIVOT>2.0.CO;2.

Chen, L., T. Duan, and W. Li, 1987: The variation of the atmospheric heat source and the budget of atmospheric energy on the Qinghai-Xizang Plateau during summer 1979 (in Chinese). *Acta Meteor. Sin.*, **43**, 1–12.

Dee, D. P., and Coauthors, 2011: The ERA-Interim reanalysis: Configuration and performance of the data assimilation system. *Quart. J. Roy. Meteor. Soc.*, **137**, 553–597, doi:10.1002/qj.828.

Dethof, A., A. O'Neill, J. M. Slingo, and H. G. J. Smit, 1999: A mechanism for moistening the lower stratosphere involving the Asian summer monsoon. *Quart. J. Roy. Meteor. Soc.*, **125**, 1079–1106, doi:10.1002/qj.1999.49712555602.

Flohn, H., 1957: Large-scale aspects of the "summer monsoon" in South and East Asia. *J. Meteor. Soc. Japan*, **35A**, 180–186.

Fu, R., and Coauthors, 2006: Short circuit of water vapor and polluted air to the global stratosphere by convective transport over the Tibetan Plateau. *Proc. Natl. Acad. Sci. USA*, **103**, 5664–5669, doi:10.1073/pnas.0601584103.

Huang, G., K. Hu, and S.-P. Xie, 2010: Strengthening of tropical Indian Ocean teleconnection to the northwest Pacific since the mid-1970s: An atmospheric GCM study. *J. Climate*, **23**, 5294–5304, doi:10.1175/2010JCLI3577.1.

——, X. Qu, and K. Hu, 2011: The impact of the tropical Indian Ocean on South Asian High in boreal summer. *Adv. Atmos. Sci.*, **28**, 421–432, doi:10.1007/s00376-010-9224-y.

Huang, R., and F. Sun, 1992: Impacts of the tropical western Pacific on the East Asian summer monsoon. *J. Meteor. Soc. Japan*, **70**, 243–256.

——, J. Chen, L. Wang, and Z. Lin, 2012: Characteristics, processes, and causes of the spatio-temporal variabilities of the East Asian monsoon system. *Adv. Atmos. Sci.*, **29**, 910–942, doi:10.1007/s00376-012-2015-x.

Jiang, X., Y. Li, S. Yang, and R. Wu, 2011: Interannual and interdecadal variations of the South Asian and western Pacific subtropical highs and their relationships with Asian-Pacific summer climate. *Meteor. Atmos. Phys.*, **113**, 171–180, doi:10.1007/s00703-011-0146-8.

Jin, Q., X.-Q. Yang, X.-G. Sun, and J.-B. Fang, 2013: East Asian summer monsoon circulation structure controlled by feedback of condensational heating. *Climate Dyn.*, **41**, 1885–1897, doi:10.1007/s00382-012-1620-9.

Kanamitsu, M., and T. N. Krishnamurti, 1978: Northern summer tropical circulations during drought and normal rainfall months. *Mon. Wea. Rev.*, **106**, 331–347, doi:10.1175/1520-0493(1978)106<0331:NSTCDD>2.0.CO;2.

Krishnamurti, T., 1973: Tibetan high and upper tropospheric tropical circulations during northern summer. *Bull. Amer. Meteor. Soc.*, **54**, 1234–1249.

Liu, Y., and G. Wu, 2004: Progress in the study on the formation of the summertime subtropical anticyclone. *Adv. Atmos. Sci.*, **21**, 322–342, doi:10.1007/BF02915562.

——, ——, H. Liu, and P. Liu, 2001: Condensation heating of the Asian summer monsoon and the subtropical anticyclone in the Eastern Hemisphere. *Climate Dyn.*, **17**, 327–338, doi:10.1007/s003820000117.

——, ——, and R. Ren, 2004: Relationship between the subtropical anticyclone and diabatic heating. *J. Climate*, **17**, 682–698, doi:10.1175/1520-0442(2004)017<0682:RBTSAA>2.0.CO;2.

——, B. Hoskins, and M. Blackburn, 2007: Impact of Tibetan orography and heating on the summer flow over Asia. *J. Meteor. Soc. Japan*, **85B**, 1–19, doi:10.2151/jmsj.85B.1.

——, G. Wu, J. Hong, B. Dong, A. Duan, Q. Bao, and L. Zhou, 2012: Revisiting Asian monsoon formation and change associated with Tibetan Plateau forcing: II. Change. *Climate Dyn.*, **39**, 1183–1195, doi:10.1007/s00382-012-1335-y.

——, J. Hu, B. He, Q. Bao, A. Duan, and G. Wu, 2013: Seasonal evolution of subtropical anticyclones in the climate system model FGOALS-s2. *Adv. Atmos. Sci.*, **30**, 593–606, doi:10.1007/s00376-012-2154-0.

Liu, Y. Y., and Y. H. Ding, 2008: Analysis and numerical simulations of the teleconnection between Indian summer monsoon and precipitation in north China. *Acta Meteor. Sin.*, **22**, 489–501.

Lu, R., and Z. Lin, 2009: Role of subtropical precipitation anomalies in maintaining the summertime meridional teleconnection over the western North Pacific and East Asia. *J. Climate*, **22**, 2058–2072, doi:10.1175/2008JCLI2444.1.

Luo, H., and M. Yanai, 1984: The large-scale circulation and heat sources over the Tibetan Plateau and surrounding areas during the early summer of 1979. Part II: Heat and moisture budgets. *Mon. Wea. Rev.*, **112**, 966–989, doi:10.1175/1520-0493(1984)112<0966:TLSCAH>2.0.CO;2.

Luo, S., Z. Qian, and Q. Wang, 1982: The climatic and synoptical study about the relation between the Qinghig-Xizang High pressure on the 100 mb surface and the flood and drought in East China in summer (in Chinese). *Plateau Meteor.*, **1**, 1–10.

Mason, R. B., and C. E. Anderson, 1963: The development and decay of the 100-mb summer time anticyclone over southern Asia. *Mon. Wea. Rev.*, **91**, 3–12, doi:10.1175/1520-0493(1963)091<0003:TDADOT>2.3.CO;2.

Park, M., W. J. Randel, L. K. Emmons, P. F. Bernath, K. A. Walker, and C. D. Boone, 2008: Chemical isolation in the Asian monsoon anticyclone observed in Atmospheric Chemistry Experiment (ACE-FTS) data. *Atmos. Chem. Phys.*, **8**, 757–764, doi:10.5194/acp-8-757-2008.

Qian, Y., Q. Zhang, Y. Yao, and X. Zhang, 2002: Seasonal variation and heat preference of the South Asia high. *Adv. Atmos. Sci.*, **19**, 821–836, doi:10.1007/s00376-002-0047-3.

Qu, X., and G. Huang, 2012: An enhanced influence of tropical Indian Ocean on the South Asia high after the late 1970s. *J. Climate*, **25**, 6930–6941, doi:10.1175/JCLI-D-11-00696.1.

——, ——, K. Hu, S.-P. Xie, Y. Du, X.-T. Zheng, and L. Liu, 2015: Equatorward shift of the South Asian high in response to anthropogenic forcing. *Theor. Appl. Climatol.*, **119**, 113–122, doi:10.1007/s00704-014-1095-1.

Randel, W. J., and M. Park, 2006: Deep convective influence on the Asian summer monsoon anticyclone and associated tracer variability observed with Atmospheric Infrared Sounder (AIRS). *J. Geophys. Res.*, **111**, D12314, doi:10.1029/2005JD006490.

Reiter, E. R., and D.-Y. Gao, 1982: Heating of the Tibet Plateau and movements of the South Asian high during spring. *Mon. Wea. Rev.*, **110**, 1694–1711, doi:10.1175/1520-0493(1982)110<1694:HOTTPA>2.0.CO;2.

Ren, R., Y. Liu, and G. Wu, 2007: Impact of South Asia High on the short-term variation of the subtropical anticyclone over western Pacific in July 1998 (in Chinese). *Acta Meteor. Sin.*, **65**, 183–197.

Rodwell, M. J., and B. J. Hoskins, 1996: Monsoons and the dynamics of deserts. *Quart. J. Roy. Meteor. Soc.*, **122**, 1385–1404, doi:10.1002/qj.49712253408.

——, and ——, 2001: Subtropical anticyclones and summer monsoons. *J. Climate*, **14**, 3192–3211, doi:10.1175/1520-0442(2001)014<3192:SAASM>2.0.CO;2.

Schneider, U., A. Becker, P. Finger, A. Meyer-Christoffer, M. Ziese, and B. Rudolf, 2014: GPCC's new land surface precipitation climatology based on quality-controlled in situ data and its role in quantifying the global water cycle. *Theor. Appl. Climatol.*, **115**, 15–40, doi:10.1007/s00704-013-0860-x.

Smith, T. M., R. W. Reynolds, T. C. Peterson, and J. Lawrimore, 2008: Improvements to NOAA's historical merged land–ocean surface temperature analysis (1880–2006). *J. Climate*, **21**, 2283–2296, doi:10.1175/2007JCLI2100.1.

Sugimoto, S., and K. Ueno, 2012: Role of mesoscale convective systems developed around the eastern Tibetan Plateau in the eastward expansion of an upper tropospheric high during the monsoon season. *J. Meteor. Soc. Japan*, **90**, 297–310, doi:10.2151/jmsj.2012-209.

Tao, S.-Y., and F.-K. Zhu, 1964: The 100-mb flow patterns in southern Asia in summer and its relation to the advance and

retreat of the west-Pacific subtropical anticyclone over the Far East (in Chinese). *Acta Meteor. Sin.*, **34**, 385–396.

——, and Y.-H. Ding, 1981: Observational evidence of the influence of the Qinghai-Xizang (Tibet) Plateau on the occurrence of heavy rain and severe convective storms in China. *Bull. Amer. Meteor. Soc.*, **62**, 23–30, doi:10.1175/1520-0477(1981)062<0023:OEOTIO>2.0.CO;2.

——, and J. Wei, 2006: The westward, northward advance of the subtropical high over the west Pacific in summer (in Chinese). *J. Appl. Meteor. Sci.*, **17**, 513–525.

Tiedtke, M., 1989: A comprehensive mass flux scheme for cumulus parameterization in large-scale models. *Mon. Wea. Rev.*, **117**, 1779–1800, doi:10.1175/1520-0493(1989)117<1779:ACMFSF>2.0.CO;2.

Wang, B., and Z. Fan, 1999: Choice of South Asian summer monsoon indices. *Bull. Amer. Meteor. Soc.*, **80**, 629–638, doi:10.1175/1520-0477(1999)080<0629:COSASM>2.0.CO;2.

——, Z. Wu, J. Li, J. Liu, C.-P. Chang, Y. Ding, and G. Wu, 2008: How to measure the strength of the East Asian summer monsoon. *J. Climate*, **21**, 4449–4463, doi:10.1175/2008JCLI2183.1.

——, B. Xiang, and J.-Y. Lee, 2013: Subtropical high predictability establishes a promising way for monsoon and tropical storm predictions. *Proc. Natl. Acad. Sci. USA*, **110**, 2718–2722, doi:10.1073/pnas.1214626110.

Wang, L., S. Guo, J. He, Z. Guan, and B. Liu, 2013: Circulation differences and possible mechanism underlying the South Asia high establishment from April to May in the early or delayed establishment years (in Chinese). *Chin. J. Atmos. Sci.*, **37**, 1165–1178.

Watanabe, M., and M. Kimoto, 2000: Atmosphere-ocean thermal coupling in the North Atlantic: A positive feedback. *Quart. J. Roy. Meteor. Soc.*, **126**, 3343–3369, doi:10.1002/qj.49712657017; Corrigendum, **127**, 733–734, doi:10.1002/qj.49712757223.

Wei, W., R. S. Zhang, and M. Wen, 2012: Meridional variation of South Asian High and its relationship with the summer precipitation over China (in Chinese). *J. Appl. Meteor. Sci.*, **23**, 650–659.

——, R. H. Zhang, M. Wen, X. Y. Rong, and T. Li, 2014: Impact of Indian summer monsoon on the South Asian High and its influence on summer rainfall over China. *Climate Dyn.*, **43**, 1257–1269, doi:10.1007/s00382-013-1938-y.

——, ——, ——, B.-J. Kim, and J.-C. Nam, 2015: Interannual variation of the South Asian high and its relation with Indian and East Asian summer monsoon rainfall. *J. Climate*, **28**, 2623–2634, doi:10.1175/JCLI-D-14-00454.1.

Wu, B., T. Li, and T. Zhou, 2010: Relative contributions of the Indian Ocean and local SST anomalies to the maintenance of the western North Pacific anomalous anticyclone during the El Niño decaying summer. *J. Climate*, **23**, 2974–2986, doi:10.1175/2010JCLI3300.1.

Wu, G., and H. Liu, 1995: Neighborhood response of rainfall to tropical sea surface temperature anomalies. Part I: Numerical experiment (in Chinese). *Chin. J. Atmos. Sci.*, **19**, 422–434.

——, and Y. Liu, 2000: Thermal adaptation, overshooting, dispersion, and subtropical anticyclone. Part I: Thermal adaptation and overshooting (in Chinese). *Chin. J. Atmos. Sci.*, **24**, 433–446.

——, and ——, 2003: Summertime quadruplet heating pattern in the subtropics and the associated atmospheric circulation. *Geophys. Res. Lett.*, **30**, 1201, doi:10.1029/2002GL016209.

——, F. Sun, J. Wang, and X. Wang, 1995: Neighborhood response of rainfall to tropical sea surface temperature anomalies. Part II: Data analysis (in Chinese). *Chin. J. Atmos. Sci.*, **19**, 663–676.

——, Y. Liu, X. Zhu, W. Li, R. Ren, A. Duan, and X. Liang, 2009: Multi-scale forcing and the formation of subtropical desert and monsoon. *Ann. Geophys.*, **27**, 3631–3644, doi:10.5194/angeo-27-3631-2009.

——, ——, B. He, Q. Bao, A. Duan, and F.-F. Jin, 2012: Thermal controls on the Asian summer monsoon. *Sci. Rep.*, **2**, 404, doi:10.1038/srep00404.

——, B. He, Y. Liu, Q. Bao, and R. Ren, 2015: Location and variation of the summertime upper-troposphere temperature maximum over South Asia. *Climate Dyn.*, **45**, 2757–2774, doi:10.1007/s00382-015-2506-4.

Xie, S.-P., K. Hu, J. Hafner, H. Tokinaga, Y. Du, G. Huang, and T. Sampe, 2009: Indian Ocean capacitor effect on Indo–western Pacific climate during the summer following El Niño. *J. Climate*, **22**, 730–747, doi:10.1175/2008JCLI2544.1.

Yanai, M., S. Esbensen, and J.-H. Chu, 1973: Determination of bulk properties of tropical cloud clusters from large-scale heat and moisture budgets. *J. Atmos. Sci.*, **30**, 611–627, doi:10.1175/1520-0469(1973)030<0611:DOBPOT>2.0.CO;2.

——, C. Li, and Z. Song, 1992: Seasonal heating of the Tibetan Plateau and its effects on the evolution of the Asian summer monsoon. *J. Meteor. Soc. Japan*, **70**, 319–351.

Yang, J., Q. Liu, S.-P. Xie, Z. Liu, and L. Wu, 2007: Impact of the Indian Ocean SST basin mode on the Asian summer monsoon. *Geophys. Res. Lett.*, **34**, L02708, doi:10.1029/2006GL028571.

Ye, D., and Y. Gao, 1979: *Meteorology of Tibetan Plateau* (in Chinese). Science Press, 278 pp.

Yeh, T.-C., S.-W. Lou, and P.-C. Chu, 1957: The wind structure and heat balance in the lower troposphere over Tibetan Plateau and its surroundings (in Chinese). *Acta Meteor. Sin.*, **28**, 108–121.

Zhang, P., S. Yang, and V. E. Kousky, 2005: South Asian high and Asian-Pacific-American climate teleconnection. *Adv. Atmos. Sci.*, **22**, 915–923, doi:10.1007/BF02918690.

Zhang, P. F., G. Li, X. Fu, Y. Liu, and L. Li, 2014: Clustering of Tibetan Plateau vortices by 10–30-day intraseasonal oscillation. *Mon. Wea. Rev.*, **142**, 290–300, doi:10.1175/MWR-D-13-00137.1.

Zhang, Q., and G. Wu, 2001: The large area flood and drought over Yangtze River Valley and its relation to the South Asia High (in Chinese). *Acta Meteor. Sin.*, **59**, 569–577.

——, ——, and Y. Qian, 2002: The bimodality of the 100 hPa South Asia High and its relationship to the climate anomaly over East Asia in summer. *J. Meteor. Soc. Japan*, **80**, 733–744, doi:10.2151/jmsj.80.733.

Zhang, R., 2001: Relations of water vapor transport from Indian monsoon with that over East Asia and the summer rainfall in China. *Adv. Atmos. Sci.*, **18**, 1005–1017.

——, A. Sumi, and M. Kimoto, 1999: A diagnostic study of the impact of El Niño on the precipitation in China. *Adv. Atmos. Sci.*, **16**, 229–241, doi:10.1007/BF02973084.

Zhao, P., Y. Zhu, and R. Zhang, 2007: An Asian–Pacific teleconnection in summer tropospheric temperature and associated Asian climate variability. *Climate Dyn.*, **29**, 293–303, doi:10.1007/s00382-007-0236-y.

——, X. Zhang, Y. Li, and J. Chen, 2009: Remotely modulated tropical-North Pacific ocean–atmosphere interactions by the South Asian high. *Atmos. Res.*, **94**, 45–60, doi:10.1016/j.atmosres.2009.01.018.